Alzheimer's & Dementia: Diagnosis, Assessment & Disease Monitoring 9 (2017) 41-50

Neuroimaging

Entorhinal and transentorhinal atrophy in mild cognitive impairment using longitudinal diffeomorphometry

Daniel J. Tward[a,b,*], Chelsea S. Sicat[a], Timothy Brown[a], Arnold Bakker[c], Michela Gallagher[d], Marilyn Albert[e], Michael Miller[a,b,f], for the Alzheimer's Disease Neuroimaging Initiative

[a]Center for Imaging Science, Johns Hopkins University, Baltimore, MD, USA
[b]Department of Biomedical Engineering, Johns Hopkins University, Baltimore, MD, USA
[c]Department of Psychiatry and Behavioral Sciences, Johns Hopkins University, Baltimore, MD, USA
[d]Department of Psychological and Brain Sciences, Johns Hopkins School of Arts and Sciences, Baltimore, MD, USA
[e]Department of Neurology, Johns Hopkins University School of Medicine, Baltimore, MD, USA
[f]Kavli Neuroscience Discovery Institute, Johns Hopkins University, Baltimore, MD, USA

Abstract

Introduction: Autopsy findings have shown the entorhinal cortex and transentorhinal cortex are among the earliest sites of accumulation of pathology in patients developing Alzheimer's disease.
Methods: Here, we study this region in subjects with mild cognitive impairment (n = 36) and in control subjects (n = 16). The cortical areas are manually segmented, and local volume and shape changes are quantified using diffeomorphometry, including a novel mapping procedure that reduces variability in anatomic definitions over time.
Results: We find significant thickness and volume changes localized to the transentorhinal cortex through high field strength atlasing.
Discussion: This demonstrates that in vivo neuroimaging biomarkers can detect these early changes among subjects with mild cognitive impairment.

Keywords: Entorhinal cortex; Mild cognitive impairment; Braak staging; Diffeomorphometry; Shape analysis; Longitudinal analysis

1. Background

The anatomic localization of the early pathologic changes associated with Alzheimer's disease (AD) aligns with the clinical presentation of most patients in the early symptomatic phase of AD. By clinical, cognitive, and functional criteria, mild cognitive impairment (MCI) is considered an intermediate state between individuals who are cognitively normal and those with a clinical diagnosis of dementia [1,2]. Impairment of episodic memory, that is, the ability to acquire and retain new information about life events, that is greater than expected for a person's age is most commonly observed in subjects with MCI who progress to AD and has been used to define a subtype of MCI called amnestic MCI [3]. Quantitative studies of autopsied brains from well-characterized patients at this phase of AD have demonstrated a substantial loss of neurons in the entorhinal cortex (ERC) [4–6]. A broad consensus now exists on this locus for early neurodegeneration and the subsequent spread of pathology along connectional pathways as disease progresses causing further symptomatic worsening through the stages of dementia.

Against this background, localized anatomic change in the medial temporal lobe observed using structural magnetic resonance imaging (MRI) has provided an indirect measure of neuronal injury [7,8]. In particular, entorhinal cortical atrophy has been identified as one of the MRI measures that predicts longitudinal progression among symptomatic cases, with greater atrophy associated with greater clinical disease severity [9–12] (also see recent review [13]). ERC atrophy

*Corresponding author. Tel.: +1-410-516-3826; Fax: +1-410-516-4594.
E-mail address: dtward@cis.jhu.edu

http://dx.doi.org/10.1016/j.dadm.2017.07.005

detected by MRI has also been predictive of progression from normal cognition to MCI [14]. Such atrophy has been associated with impairment on multiple memory tests confirming that this atrophy has clinical relevance for patients [15].

The field of computational anatomy [16] has been working toward addressing the need for quantitative, well-researched, standardized structural imaging biomarkers for neurodegenerative disease. Patterns of atrophy at the population and individual level are described quantitatively by constructing smooth mappings (diffeomorphisms) that identify correspondences between a well-characterized template image and a given patient image. Properties of these mappings, such as how much they expand or contract, are used to give a quantitative description of biological change. These tools have been previously applied to a study of the medial temporal lobe [17], where significant atrophy was found present in the most lateral portion of the ERC. In this study, we use structural MRI to investigate the cortical region further lateral, the transentorhinal cortex (TEC), which is one of the sites of the earliest detected pathology as reported by Braak and Braak [18].

Because of its proximity to meninges and the oculomotor nerve, as well as the fact that its definition is specified by distant landmarks rather than local contrast changes [19], this area is difficult for automatic segmentation techniques. Although some techniques [20] are addressing these concerns, we choose to use manual segmentations in this study. In this context, one important source of variability is the consistency of segmentations over time.

Our approach to overcoming this limitation is to develop a longitudinal filtering procedure, passing a template segmentation through each time point along a continuous trajectory. This allows data to be shared between various time points, removing noise associated with variable structure definition over time. The trajectory we choose is modeled by two geodesics through the space of diffeomorphisms, one from template to baseline and other from baseline through each follow up. This leads to a procedure that is essentially linear regression through the high-dimensional space of images.

We study a sample of subjects from the Alzheimer's disease neuroimaging initiative (ADNI) who are cognitively normal or have MCI by clinical and cognitive criteria at baseline. We measure volume changes over time to compute volumetric atrophy rate due to MCI, and we measure local volume and thickness over time to compute the spatial distribution of these changes. Regions where atrophy is significantly different between groups are identified using permutation testing, controlling for multiple comparisons using the maximum statistic.

2. Methods

2.1. Subjects

Data used in the preparation of this article were obtained from the ADNI database (adni.loni.usc.edu). MRI scans from subjects who met ADNI criteria for MCI at baseline were selected for analysis. Inclusion criteria for subjects with MCI included evidence of impaired performance on Logical Memory Subtest of the Wechsler Memory Scale (based on age and education adjusted norms), a score of clinical dementia rating (CDR) $\geq$0.5, and a clinical diagnosis of MCI. The MCI subjects were all selected to be amyloid β positive based on cerebrospinal fluid cutoff values established by the ADNI Biospecimen Core (i.e., less than a cutoff score of 192 pg/mL) [21] and age between 55 and 85 years.

The criteria for control status in ADNI included evidence of performance within the normal range on the Logical Memory Subtest of the Wechsler Memory Scale (based on age and education adjusted norms), a score of CDR = 0, and the absence of a clinical diagnosis of MCI or dementia. Control subjects were included only if they were amyloid β negative (greater than a cutoff of 192 pg/mL). In total, 36 subjects with amnestic MCI and 16 control subjects were selected. Their baseline demographics and cognitive scores are summarized in Table 1.

2.2. Manual segmentation protocol

Analysis included subjects who had no discontinuity in their collateral sulcus (type I variant described in [22] and further discussed in [23]) and was restricted to the left side of the MRI scan. Most subjects examined were found to have this anatomic variant on the left side, but many had alternative variants on the right. Only subjects scanned for at least three time points for more than 2 years were included. Most were scanned at 6, 12, and 24 months after baseline. Data for one subject is shown in Fig. 1 left panel. We denote the ith subject's jth scan time as t_{ij}.

ERC and TEC were segmented manually, using anatomic boundaries described in [19]. As seen in the coronal plane, the boundaries can be described by

- Rostral: 4 mm rostral to hippocampal head
- Caudal: 2 mm caudal to gyrus intralimbicus
- Medial: As far as visible gray/white boundary
- Lateral: Deepest part of collateral sulcus

Segmentations were performed in Seg3D version 1 [24]. One example is shown in the coronal plane in Fig. 1 right

Table 1
Baseline demographic information for control and mild cognitive impairment (MCI) groups

Parameter	Control	MCI
Number	16	36
Age	71.7 ± 6.01	72.0 ± 7.61
Female gender	43.8%	50.0%
CDR	0 ± 0	1.57 ± 0.719
Mini-Mental State Examination	29.4 ± 1.03	27.4 ± 1.77
Wechsler Memory Scale (WMS) Logical Memory (Immediate)	14.3 ± 2.27	3.42 ± 2.55
WMS Logical Memory (Delayed)	15.2 ± 3.22	7.06 ± 3.22

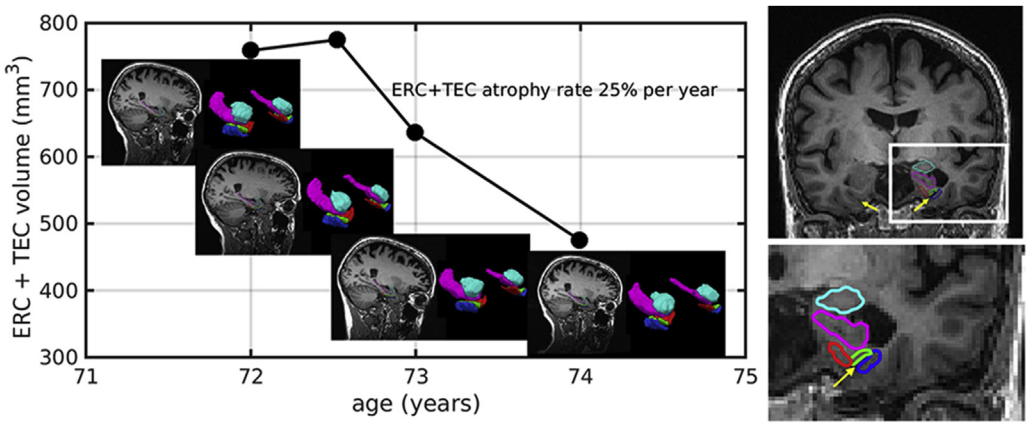

Fig. 1. Left panel: A time series for one subject with MCI is shown, with structural imaging together with medial temporal lobe segmentations (magenta, hippocampus; cyan, amygdala; red, ERC; green, TEC; blue, perirhinal cortex). Volumetry of the ERC + TEC is shown indicating a trend of 25% atrophy per year for more than 2 years. Note that this subject was selected for illustrative purposes and shows atrophy much larger than the average for the population as a whole, which is 5.6% per year. Right panel: Coronal view of example T1 image. In the left hemisphere, segmentations of the hippocampus (magenta), amygdala (cyan), ERC (red), TEC (green), and perirhinal cortex (blue) are shown, with collateral sulcus indicated by a yellow arrow. The region we analyze in this work extends along the medial bank to the deepest part of the sulcus. Bottom panel shows close up of left temporal lobe as indicated by frame. Abbreviations: ERC, entorhinal cortex; MCI, mild cognitive impairment; TEC, transentorhinal cortex.

panel, together with nearby medial temporal lobe structures. Note that the region we consider extends laterally into the collateral sulcus, beyond the ERC region that has been studied previously.

Within subject images were aligned rigidly to baseline by minimizing sum of square difference between T1 voxel intensities. All segmentations were aligned to a template using four landmarks placed automatically at the corners of the ERC and TEC. The resulting manual segmentation images for patient i at time t_{ij} are denoted by J^{ij}.

2.3. Diffeomorphic image matching

We compute diffeomorphic mappings used to match a template binary segmentation image I to target binary segmentation images J^{ij} (corresponding to subject i at time t_{ij}) by integrating a time varying velocity field

$$\frac{d}{dt}\varphi_t = v_t(\varphi_t)$$

with initial condition $\varphi_t = \mathrm{Id}$ (identity). The vector fields v_t are chosen to belong to a reproducing kernel Hilbert space V, with kernel

$$K(x,x') = \frac{1}{(2\pi\sigma_b^2)^{3/2}}\exp\left(-\frac{1}{2\sigma_V^2}|x-x'|^2\right)$$

where $|\bullet|$ denotes the norm of a vector in R^3. Smoothness criteria for vector fields in the space V to generate diffeomorphic transformations are discussed in [25].

We choose to parametrize v_t by a function p_0 supported on the boundary of an atlas surface as in [26]. Describing this surface parametrically through a function $f : U \subset \mathbf{R}^2 \to \mathbf{R}^3$, our velocity can be written as

$$v(x) = \int_U K(x,f(u))p_0(u)\,du$$

This representation is optimal when images to be matched are piecewise constant functions [27] and is a parsimonious model otherwise. The surface f is represented as a discrete triangulated surface by specifying a list of vertices and faces. For a further reduction in complexity, we restrict ourselves to modeling p_0, the initial condition to a geodesic flow given by

$$\frac{d}{dt}f_t(u) = v_t(f_t(u)), \qquad \frac{d}{dt}p_t(u) = -Dv_t^T(f_t(u))$$

as derived in [27]. Here D_v denotes the matrix of partial derivatives whose ith row is the gradient vector of the ith component of v, and T denotes the transpose.

The binary segmentation images to be matched are deformed using functional composition with the inverse $I_t = I_0(\varphi_t^{-1})$. The template image I_0 and corresponding triangulated surface f_0 are estimated from the population in a Bayesian setting as originally described in [28,29] with details discussed in [30]. Our initial guess (hypertemplate) used as an input to the template estimation algorithm was created by (1) computing the voxel-by-voxel average of each baseline rigidly aligned segmentation, (2) constructing a smooth triangulated surface contouring this average image, and (3) constructing a binary image from this surface by setting inside voxels to 1 and outside voxels to 0. The resulting template used is a deformation of this initial guess that is close to each member of the population (a population average in the Riemannian sense).

To summarize, in this work we use binary images (I) for our cost function's matching term, and we use a surface (f) to parameterize their deformation. The two are related because this surface contours the deforming atlas image. Unlike

discrete images, our surface provides smoothness and well-defined normals, allowing it to be used as an interpretable and parsimonious representation.

2.4. Longitudinal mapping

We overcome variability in anatomic definitions over time by mapping our template simultaneously onto each scan in a time series. Our approach is to define two geodesic trajectories parametrized by the functions $p^0$and p^1. This results in diffeomorphisms φ_t^0 (from template to baseline), indexed by $t\in[0,1]$, and φ_t^1 from baseline through the time series, indexed by $t\in[t_1,t_n]$with $\varphi_{t_1}^1=\mathrm{Id}$.

We are given a template segmentation I_0 and a target family of target segmentations J^{ij} at times $t_{ij}$for $j\in\{1,\ldots,N_i\}$. We seek to minimize the data fidelity function

$$\sum_{i=1}^{N}\frac{1}{2\sigma_I^2}\left\|I_0\left(\varphi_1^{0,-1}\circ\varphi_{t_{ij}}^{1,-1}(\bullet)\right)-J^{ij}\right\|_{L_2}^2$$

where$\|\bullet\|_{L_2}$is the L_2 norm of a scalar-valued function, defined by $\|I\|_{L_2}=\int_\Omega|I(x)|^2\,dx$ and σ_I^2 is a positive real number controlling the relative weight of the data fidelity term in our cost function.

In addition, we include regularization terms of the form

$$\|p\|_{V^*}^2\doteq\int_{U\times U}p^T(u)K(f(u),f(u'))p(u')\,du\,du'$$

This is the norm of the initial velocity vector field on our reproducing kernel Hilbert space of smooth functions. See [31] for details. Optimal mappings are computed by minimizing the cost function

$$C(p^0,p^1)=\frac{1}{2\sigma_0^2}\left\|p_0^0\right\|_{V^*}^2+\frac{1}{2\sigma_1^2}\left\|p_0^1\right\|_{V^*}^2+\sum_{i=1}^{N}\frac{1}{2\sigma_I^2}\left\|I_0\left(\varphi_{t_{ij}}^{1,-1}\circ\varphi_1^{0,-1}(\bullet)\right)-J^{ij}\right\|_{L_2}^2$$

for σ_0^2 and σ_1^2 positive real numbers controlling the relative weight of each regularization term. This implementation is discussed in [30] with computational details including graphics processing unit performance discussed in [32].

2.5. Global volume measurement

At each time point, we measure the volume of the region by summing voxels in the segmentation images and multiplying by the voxel size. When images are not binary due to linear interpolation on rigid alignment, we sum their interpolated value, which we interpret as a voxel that is fractionally filled by the anatomy of interest.

2.6. Local measurements

Local atrophy measurements are calculated from properties of the mappings, $\varphi_{t_{ij}}^1(\varphi_1^0)$. The local change in volume between template and subject i time j is estimated at each vertex x_k of our triangulated surface as the determinant of the Jacobian of the mapping $\left|D\varphi_{t_{ij}}^1(\varphi_1^0(x_k))\right|$.

The local change in thickness is estimated as the ratio of the Jacobian determinant to the local change in surface area ("volume equals surface area times thickness"). This approach is valid when the template is a thin laminar structure like the ERC and TEC. Local surface area change is estimated by computing, for each triangular face of our template, the deformed triangle area divided by the template triangle area. This measure is interpolated from faces to vertices by assigning to each vertex the sum of 1/3 of the value at its neighboring faces. This choice of interpolation preserves the total area.

2.7. Mixed-effects modeling

We estimate the atrophy rate using a log-linear mixed-effects model, treating gender as a fixed effect and patient-to-patient variability as a random effect. With y_{ij} a volumetric measurement (either the volume of the structure or measure of local thickness or volume change at some vertex on our template) for subject i and scan j, the model can be written as

$$\log y_{ij}=a+b(\text{elapsed time})_{ij}+(MCI)_i\left(a'+b'(\text{elapsed time})_{ij}\right)+c\,(\text{female})_i+e_i+\varepsilon_{ij}\tag{1}$$

where the constants a, b, and c are estimated by maximum likelihood. Here e_i is the patient-specific random effect with expected value to be estimated and ε_{ij} is the measurement noise. Both are assumed to be normally distributed with zero mean, and variance to be estimated by maximum likelihood. Here $\mathrm{MCI_i}$ is a binary variable indicating whether subject i has MCI or is a control. The same is true for the variable female_i. We choose a log-linear model

because each volumetric measure analyzed is constrained to be positive.

The value $b + b'\text{MCI}_i$ is related to annual atrophy rate percentage by the equation

$$\text{Atrophy rate} = 100(1 - \exp(b + b'\text{MCI}_i))$$

For small values this is approximately atrophy rate $= 100(-b - b'\,\text{MCI}_i)$, so for example a value of $b = -0.02$ corresponds to about 2% tissue loss per year.

We test the null hypothesis that $a' = b' = 0$, using a likelihood ratio test statistic and permutation testing with 10,000 permutations. The nuisance variable c is estimated under the null hypothesis, and permutation testing is performed on the residuals. We address the multiple comparison problem by using the maximum statistic to control familywise error rate at 5% as described in [33].

2.8. High field atlasing

We visualize our results with respect to an atlas imaged at high field strength where a partition of the ERC and surrounding area could be determined using the protocol described in [19,34]. An ex vivo specimen of a patient with AD was scanned at 11 T and manually segmented as shown in Fig. 2. Details of this procedure are also described in [35].

Note that the nomenclature in this region is used differently by different authors. Our high field partition contains a region referred to the sulcal subfield of the ERC in [34], which is referred to as the TEC in [19] and throughout our work.

3. Results

3.1. Manual segmentations and longitudinal filtering

Examples of the anatomic structures used in our analysis are shown in Fig. 3. Our triangulated surface template is shown at left in cyan, and isocontours of our manual segmentations are shown in red. The results of our mapping algorithm are shown in blue.

To demonstrate the range of atrophy in the subjects, Fig. 3 top shows a case with no volume loss on top, and a case with substantial volume loss on the bottom. To demonstrate our mapping method's ability to filter out variability, Fig. 3 bottom shows a case with low variability on top and high variability on the bottom. Note that in the low variability case, defects in the segmentation, such as holes, are still filtered out. In the high variability case, variations in the rostral-caudal extent of the cortex are filtered out.

3.2. Volume results

Measurements of the total volume of ERC and TEC are shown as a function of elapsed time in Fig. 4. The left side shows raw measurements. The right side shows data corrected for the effect of gender and patient variability (the expected value of e_i) under the alternate hypothesis that there is a difference between the control and MCI group. The null hypothesis is rejected with $P = .002$.

3.3. Local atrophy results

Our estimated local thickness atrophy rate is shown in Fig. 5 left panel. The top row shows the atrophy for subjects with MCI ($b+b'$ from (1)). The second row shows the difference between MCI and control groups (b' only). The third row shows the same, but only in regions where we can reject the null hypothesis ($a' = b' = 0$) with an family-wise error rate of 5%. The final row shows P values corrected for multiple comparisons. The global null hypothesis of no difference between MCI and control groups is rejected with $P = .0002$.

The estimated volume atrophy rate is shown in Fig. 5 right panel. The global null hypothesis is rejected with

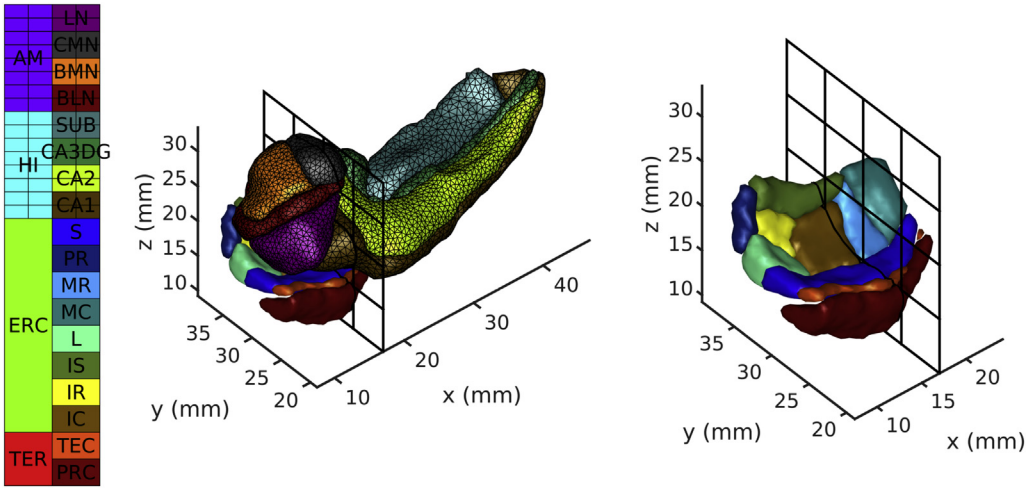

Fig. 2. High field atlas constructed from an ex vivo specimen with Alzheimer's disease scanned in an 11 T magnetic resonance imaging scanner. Subfields of the amygdala, hippocampus, entorhinal cortex, and transentorhinal region are indicated in the legend to the left.

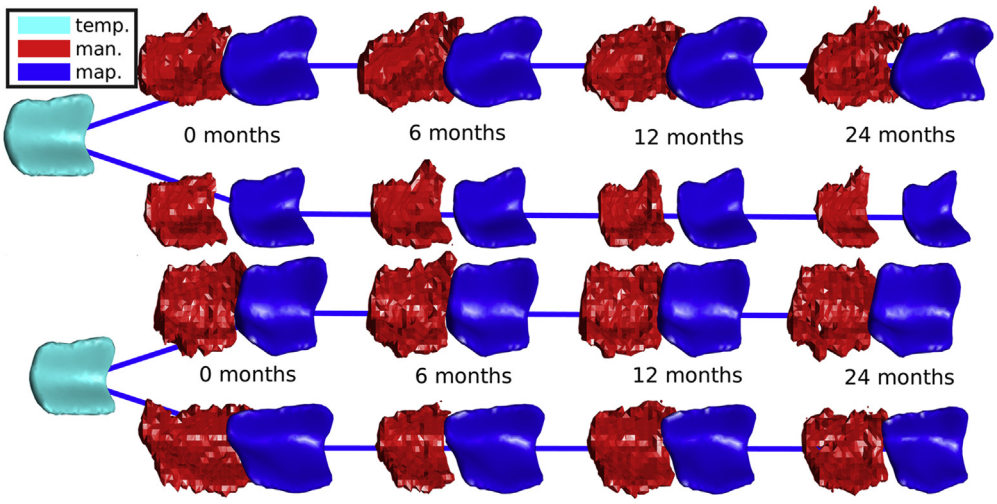

Fig. 3. Examples of manual segmentations (red) and outputs of our mapping procedure (blue) over time (left to right). A superior view is shown with medial up and rostral right. Top to bottom: low atrophy, high atrophy, low variability, high variability.

$P = .0043$. Group differences are found in roughly the same region for both change in thickness and change in volume, toward the lateral side of the cortex examined. The local volume change measure also shows some significant group differences more medially.

3.4. High field atlasing

These results are mapped, using the same techniques described previously but with only one time point, onto our high field atlas partition and are shown in Fig. 6. With this technique, it can be seen that most of the significant changes are localized to the TEC (referred to by some authors as the sulcal region of the ERC). Some changes are also located more medially in the lateral subfield and the intermediate caudal subfield. The local volume change measure also shows some changes in the intermediate superior subfield.

4. Discussion

This study demonstrates in vivo changes on MRI at the millimeter scale that colocalizes extremely well with neurofibrillary tangles found at autopsy in Braak stages I and II, the transentorhinal stage [18], and identifies a specific region whose atrophy could be used as an appropriately designed and standardized biomarker of disease. Measuring atrophy in this specific region at the population level may be useful for determining efficacy of disease-modifying interventions before cognitive changes occur. This contributes to a growing body of evidence that imaging biomarkers in the entorhinal region can be sensitive to changes in early AD. The quantitative nature of this work overcomes some criticisms of structural neuroimaging as a biomarker for AD as described in [36].

An important consideration that arises when using this filtering method is whether the variability being removed is because of manual segmentation noise or because of

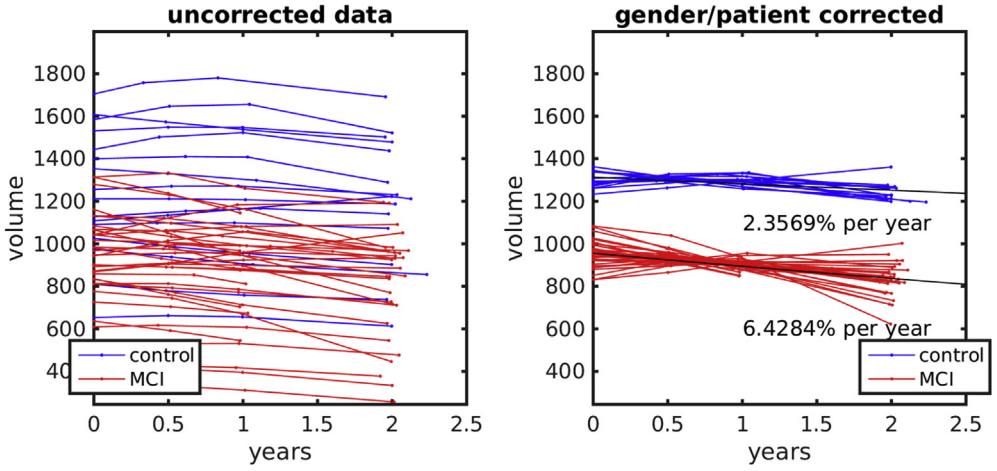

Fig. 4. Volumetry shown as a function of elapsed time with control subjects shown in blue and mild cognitive impairment (MCI) subjects shown in red. Left panel: raw data. Right panel: data corrected by the effect of gender and expected patient variability. The null hypothesis is rejected with $P = .002$.

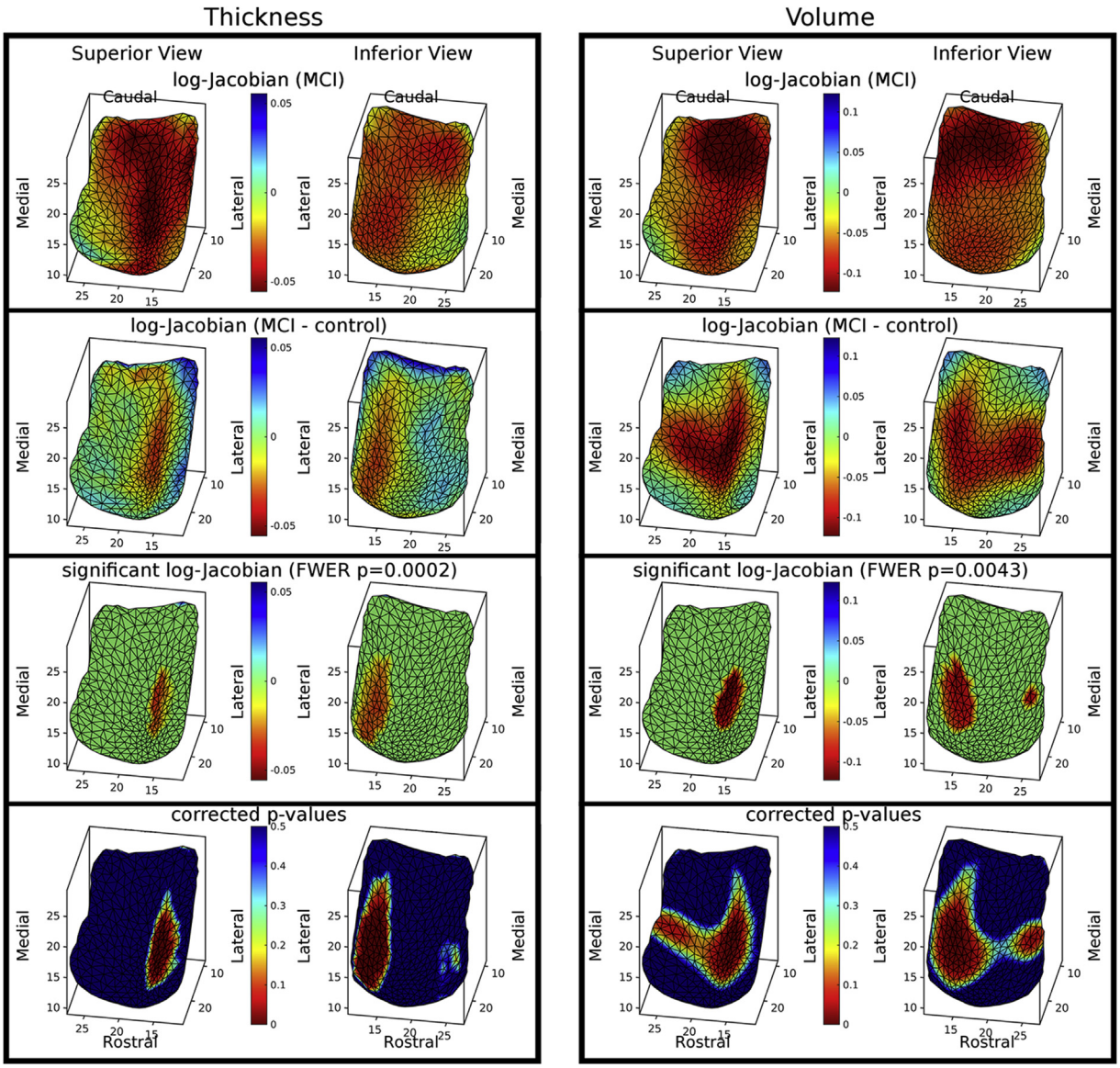

Fig. 5. Left panel: Local thickness atrophy computed from Jacobian. Right panel: Local volume atrophy computed from Jacobian. First row, atrophy rate for MCI subjects; second row, difference in atrophy rate between MCI and control groups; third row, results from second row set to zero in regions not statistically significant 5% FWER; bottom row, P values corrected for familywise error rate.

true biological variability. Filtering techniques should be considered in the context of this bias variance trade-off. We have attempted to address this by resegmenting and refiltering eight scans. From repeated segmentations we estimate a median Dice overlap (volume of intersection divided by average volume) of 0.801 for manual segmentations and 0.861 for filtered segmentations, the second being significantly improved ($P = .0078$, signed rank test). These numbers are significant given that this is a laminar structure with thickness of only a few voxels, and the large majority of errors are within one voxel. This improvement in reproducibility, together with good overall mapping accuracy, demonstrates that the procedure is likely removing noise and not the biological signal of interest. This is consistent with earlier work [37], where the cross-sectional version of this filtering procedure was shown to improve reproducibility across repeated scans and visits.

This study used two approaches to be sensitive to early structural changes in AD. First, motivated by histologic evidence, we focus our analysis on the entorhinal and transentorhinal region. Although many authors have studied the ERC, our region includes tissue lateral to most definitions of the ERC. A review of publications based on the ADNI dataset [38] describes the involvement of the ERC volume and thickness in disease progression, whereas the transentorhinal region is not discussed. Second, our method considers a detailed spatial distribution of structural changes, as opposed to analyzing thickness or volume averaged over larger regions. Although more recent work has been honing in on the transentorhinal region, such as [39] that quantifies changes in

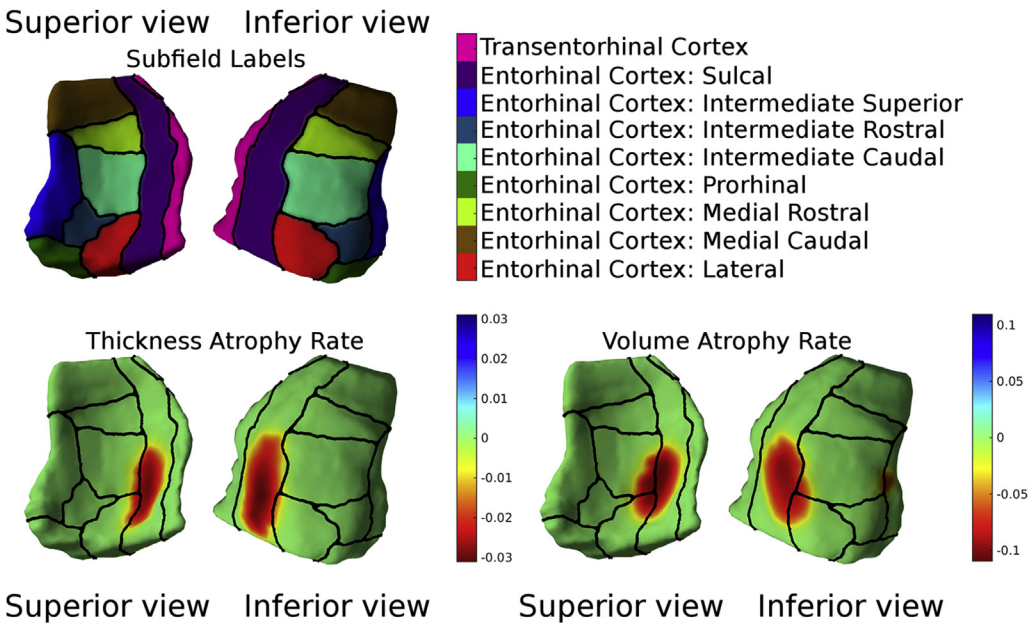

Fig. 6. Entorhinal and transentorhinal cortex partition. Bottom left: significant thickness atrophy rate; bottom right: significant volume atrophy rate.

Broadman's area 35, our analysis can detect more localized patterns of atrophy.

This work follows a trend in shape analysis in medical imaging to account for longitudinal changes explicitly. Similar approaches (known as geodesic regression) have been described in a very general setting in [40] and have been extended to hierarchical models in [41] and to aligning one time series to another [42]. In [43], several different approaches to parametrizing the trajectory in longitudinal mapping are outlined, including the two geodesic techniques used here, the piecewise geodesic technique used in [42] and higher order spline techniques. Longitudinal Freesurfer [44] provides an alternative approach to managing longitudinal data, where each scan in a time series is analyzed using a common subject-specific initialization to an optimization process. Many of these approaches are designed to allow sudden changes in the time course of the trajectory. The technique used here was designed specifically to avoid sudden changes, which in our application were likely a source of noise.

One limitation of this study is the exclusion of anatomic variants of the collateral sulcus, and our future work will expand to a larger number of subjects. However, only 16% of subjects examined did not have the type I variant on the left side.

Acknowledgments

Data used in the preparation of this article were obtained from the Alzheimer's Disease Neuroimaging Initiative (ADNI) database (adni.loni.usc.edu). As such, the investigators within the ADNI contributed to the design and implementation of ADNI and/or provided data but did not participate in the analysis or writing of this report. A complete listing of ADNI investigators can be found at http://adni.loni.usc.edu/wp-content/uploads/how_to_apply/ADNI_Acknowledgement_List.pdf. Data collection and sharing for this project was funded by the Alzheimer's Disease Neuroimaging Initiative (ADNI) (National Institutes of Health Grant U01 AG024904) and DODADNI (Department of Defense award number W81XWH-12-2-0012). ADNI is funded by the National Institute on Aging, the National Institute of Biomedical Imaging and Bioengineering, and through generous contributions from the following: AbbVie, Alzheimer's Association; Alzheimer's Drug Discovery Foundation; Araclon Biotech; BioClinica, Inc; Biogen; Bristol-Myers Squibb Company; CereSpir, Inc; Cogstate; Eisai Inc; Elan Pharmaceuticals, Inc; Eli Lilly and Company; EuroImmun; F. Hoffmann-La Roche Ltd and its affiliated company Genentech, Inc; Fujirebio; GE Healthcare; IXICO Ltd; Janssen Alzheimer Immunotherapy Research & Development, LLC; Johnson & Johnson Pharmaceutical Research & Development LLC; Lumosity; Lundbeck; Merck & Co, Inc; Meso Scale Diagnostics, LLC; NeuroRx Research; Neurotrack Technologies; Novartis Pharmaceuticals Corporation; Pfizer Inc; Piramal Imaging; Servier; Takeda Pharmaceutical Company; and Transition Therapeutics. The Canadian Institutes of Health Research is providing funds to supportADNI clinical sites in Canada. Private sector contributions are facilitated by the Foundation for the National Institutes of Health (www.fnih.org). The grantee organization is the Northern California Institute for Research and Education, and the study is coordinated by the Alzheimer's Therapeutic Research Institute at the University of Southern California. ADNI data are disseminated by the Laboratory for Neuroimaging at the University of Southern California.

This work used the Extreme Science and Engineering Discovery Environment (XSEDE) [45], which is supported by the National Science Foundation grant number ACI-1548562.
Michela Gallagher, PhD, is the founder of AgeneBio, Inc inventor of technology licensed by Johns Hopkins University to the company. She has a financial interest in the company, which is managed by the Johns Hopkins University. Michael Miller reports personal fees from AnatomyWorks, LLC, outside the submitted work, and jointly owns "AnatomyWorks". This arrangement is being managed by the Johns Hopkins University in accordance with its conflict of interest policies. Dr Miller's relationship with AnatomyWorks is being handled under full disclosure by the Johns Hopkins University.
Funding: This work was supported by the National Institutes of Health [grant number P41 EB015909]; the National Institute on Aging [grant number R01 AG048349]; the Phyllis F. Albstein Fund; and the Kavli Neuroscience Discovery Institute.

RESEARCH IN CONTEXT

1. Systematic review: The authors reviewed the literature using traditional (e.g., PubMed and Google Scholar) sources and meeting abstracts and presentations. This included both research and reviews in Alzheimer's and mild cognitive impairment definitions and pathology, as well as techniques in statistical shape analysis. These works are appropriately cited in this study.
2. Interpretation: Our findings demonstrate in vivo changes in the transentorhinal cortex in patients with amnestic mild cognitive impairment using high-resolution magnetic resonance imaging that colocalizes with accumulation of neurofibrillary tangles observed at autopsy in Braak stages I and II and identifies a specific region whose atrophy could be used as a biomarker of disease progression.
3. Future directions: The work presented in this study will be expanded to include subjects with anatomic variations in the collateral sulcus and to a larger sample size. The potential role of this approach for determining efficacy of disease-modifying interventions before cognitive changes occur will be investigated.

References

[1] Petersen RC, Smith GE, Waring SC, Ivnik RJ, Tangalos EG, Kokmen E. Mild cognitive impairment: clinical characterization and outcome. Arch Neurol 1999;56:303–8.
[2] Albert MS, DeKosky ST, Dickson D, Dubois B, Feldman HH, Fox NC, et al. The diagnosis of mild cognitive impairment due to Alzheimer's disease: recommendations from the National Institute on Aging-Alzheimer's Association workgroups on diagnostic guidelines for Alzheimer's disease. Alzheimers Dement 2011;7:270–9.
[3] Petersen RC. Mild cognitive impairment as a diagnostic entity. J Intern Med 2004;256:183–94.
[4] Gomez-Isla T, Price JL, McKeel DW Jr, Morris JC, Growdon JH, Hyman BT. Profound loss of layer II entorhinal cortex neurons occurs in very mild Alzheimer's disease. J Neurosci 1996;16:4491–500.
[5] Kordower JH, Chu Y, Stebbins GT, DeKosky ST, Cochran EJ, Bennett D, et al. Loss and atrophy of layer II entorhinal cortex neurons in elderly people with mild cognitive impairment. Ann Neurol 2001; 49:202–13.
[6] Price JL, Ko AI, Wade MJ, Tsou SK, McKeel DW, Morris JC. Neuron number in the entorhinal cortex and CA1 in preclinical Alzheimer disease. Arch Neurol 2001;58:1395–402.
[7] Atiya M, Hyman BT, Albert MS, Killiany R. Structural magnetic resonance imaging in established and prodromal Alzheimer disease: a review. Alzheimer Dis Assoc Disord 2003;17:177–95.
[8] Kantarci K, Jack CRJ. Quantitative magnetic resonance techniques as surrogate markers of Alzheimer's disease. NeuroRx 2004;1:196–205.
[9] Devanand D, Pradhaban G, Liu X, Khandji A, De Santi S, Segal S, et al. Hippocampal and entorhinal atrophy in mild cognitive impairment prediction of Alzheimer disease. Neurology 2007;68:828–36.
[10] Kerchner GA, Deutsch GK, Zeineh M, Dougherty RF, Saranathan M, Rutt BK. Hippocampal CA1 apical neuropil atrophy and memory performance in Alzheimer's disease. Neuroimage 2012; 63:194–202.
[11] Devanand D, Bansal R, Liu J, Hao X, Pradhaban G, Peterson BS. MRI hippocampal and entorhinal cortex mapping in predicting conversion to Alzheimer's disease. Neuroimage 2012;60:1622–9.
[12] La Joie R, Perrotin A, Barre L, Hommet C, Mezenge F, Ibazizene M, et al. Region-specific hierarchy between atrophy, hypometabolism, and beta-amyloid (Abeta) load in Alzheimer's disease dementia. J Neurosci 2012;32:16265–73.
[13] Duara R, Barker W, Loewenstein D, Greig MT, Rodriguez R, Goryawala M, et al. Insights into cognitive aging and Alzheimer's disease using amyloid PET and structural MRI scans. Clin Transl Imaging 2015;3:65–74.
[14] Younes L, Albert M, Miller MI, BIOCARD Research Team. Inferring changepoint times of medial temporal lobe morphometric change in preclinical Alzheimer's disease. Neuroimage Clin 2014;5:178–87.
[15] Varon D, Loewenstein DA, Potter E, Greig MT, Agron J, Shen Q, et al. Minimal atrophy of the entorhinal cortex and hippocampus: progression of cognitive impairment. Dement Geriatr Cogn Disord 2011; 31:279–83.
[16] Grenander U, Miller MI. Computational anatomy: an emerging discipline. Q Appl Math 1998;56:617–94.
[17] Miller MI, Younes L, Ratnanather JT, Brown T, Trinh H, Postell E, et al. The diffeomorphometry of temporal lobe structures in preclinical Alzheimer's disease. Neuroimage Clin 2013;3:352–60.
[18] Braak H, Braak E. Neuropathological stageing of Alzheimer-related changes. Acta Neuropathol 1991;82:239–59.
[19] Insausti R, Juottonen K, Soininen H, Insausti AM, Partanen K, Vainio P, et al. MR volumetric analysis of the human entorhinal, perirhinal, and temporopolar cortices. AJNR Am J Neuroradiol 1998;19:659–71.
[20] Xie L, Wisse LE, Das SR, Wang H, Wolk DA, Manjon JV, et al. Accounting for the confound of meninges in segmenting entorhinal and perirhinal cortices in T1-weighted MRI. Presented at the International Conference on Medical Image Computing and Computer-assisted Intervention; October, 2016.
[21] Shaw LM, Vanderstichele H, Knapik-Czajka M, Clark CM, Aisen PS, Petersen RC, et al. Cerebrospinal fluid biomarker signature in Alzheimer's disease neuroimaging initiative subjects. Ann Neurol 2009;65:403–13.
[22] Ding SL, Van Hoesen GW. Borders, extent, and topography of human perirhinal cortex as revealed using multiple modern neuroanatomical and pathological markers. Hum Brain Mapp 2010;31:1359–79.

[23] Huntgeburth SC, Petrides M. Morphological patterns of the collateral sulcus in the human brain. Eur J Neurosci 2012;35:1295–311.
[24] CIBC, Seg3D: Volumetric image segmentation and visualization. Scientific Computing and Imaging Institute (SCI). 2016. Available at: http://www.seg3d.org. Accessed April 24, 2017.
[25] Dupuis P, Grenander U, Miller MI. Variational problems on flows of diffeomorphisms for image matching. Q Appl Math 1998;56:587–600.
[26] Tward D, Miller M, Trouve A, Younes L. Parametric surface diffeomorphometry for low dimensional embeddings of dense segmentations and imagery. IEEE Trans Pattern Anal Mach Intell 2016; 39:1195–208.
[27] Miller MI, Trouve A, Younes L. Geodesic shooting for computational anatomy. J Math Imaging Vis 2006;24:209–28.
[28] Ma J, Miller MI, Trouve A, Younes L. Bayesian template estimation in computational anatomy. Neuroimage 2008;42:252–61.
[29] Ma J, Miller MI, Younes L. A Bayesian generative model for surface template estimation. J Biomed Imaging 2010;2010.
[30] Tward DJ, Sicat CS, Brown T, Bakker A, Miller MI. Reducing variability in anatomical definitions over time using longitudinal diffeomorphic mapping. Presented at the International Workshop on Spectral and Shape Analysis in Medical Imaging; October, 2016.
[31] Vaillant M, Glaunes J. Surface matching via currents. Presented at the: Biennial International Conference on Information Processing in Medical Imaging; 2005.
[32] Tward DJ, Kolasny A, Sicat CS, Brown T, Miller MI. Tools for studying populations and timeseries of neuroanatomy enabled through GPU acceleration in the computational anatomy gateway. Proceedings of the XSEDE16 Conference on Diversity, Big Data, and Science at Scale. Miami, FL: ACM; 2016.
[33] Nichols T, Hayasaka S. Controlling the familywise error rate in functional neuroimaging: a comparative review. Stat Methods Med Res 2003;12:419–46.
[34] Krimer L, Hyde T, Herman M, Saunders R. The entorhinal cortex: an examination of cyto-and myeloarchitectonic organization in humans. Cereb Cortex 1997;7:722–31.
[35] Miller MI, Ratnanather JT, Tward DJ, Brown T, Lee DS, Ketcha M, et al. Network neurodegeneration in Alzheimer's disease via MRI based shape diffeomorphometry and high-field atlasing. Front Bioeng Biotechnol 2015;3:54.
[36] Jack CR, Albert MS, Knopman DS, McKhann GM, Sperling RA, Carrillo MC, et al. Introduction to the recommendations from the National Institute on Aging-Alzheimer's Association workgroups on diagnostic guidelines for Alzheimer's disease. Alzheimers Dement 2011;7:257–62.
[37] Tward D, Jovicich J, Soricelli A, Frisoni G, Trouve A, Younes L, et al. Improved reproducibility of neuroanatomical definitions through diffeomorphometry and complexity reduction. Presented at the International Workshop on Machine Learning in Medical Imaging; 2014.
[38] Weiner M, Veitch D, Aisen P, Beckett L, Cairns N, Cedarbaum J, et al. 2014 Update of the Alzheimer's Disease Neuroimaging Initiative: a review of papers published since its inception. Alzheimers Dement 2015;11:e1–20.
[39] Wolk D, Das S, Meuller S, Weiner M, Yushkevich P. Medial temporal lobe subregionalmorphometry using high resolution MRI in Alzheimer's disease. Neurobiol Aging 2017;49:201–13.
[40] Fletcher PT. Geodesic regression and the theory of least squares on Riemannian manifolds. Int J Comput Vis 2013;105:171–85.
[41] Singh N, Hinkle J, Joshi S, Fletcher PT. Hierarchical geodesic models in diffeomorphisms. Int J Computer Vis 2016;117:70–92.
[42] Durrleman S, Pennec X, Braga J, Gerig G, Ayache N. Toward a comprehensive framework for the spatiotemporal statistical analysis of longitudinal shape data. Int J Comput Vis 2013;103:22–59.
[43] Miller MI, Trouve A, Younes L. Hamiltonian systems and optimal control in computational anatomy: 100 years since D'Arcy Thompson. Annu Rev Biomed Eng 2015;17:447–509.
[44] Reuter M, Schmansky NJ, Rosas HD, Fischl B. Within-subject template estimation for unbiased longitudinal image analysis. Neuroimage 2012;61:1402–18.
[45] Town J, Cockerill T, Dahan M, Foster I, Gaither K, Grimshaw A, et al. XSEDE: accelerating scientific discovery. Comput Sci Eng 2014; 16:62–74.